Revisiting the alignment of radio galaxies in the ELAIS-N1 field

Simonte, M.; Andernach, H.; Brüggen, M.; Best, P.N.; Osinga, E.

Astronomy & Astrophysics

Revisiting the alignment of radio galaxies in the ELAIS-N1 field[*]

M. Simonte[1] , H. Andernach[2,**], M. Brüggen[1], P. N. Best[3], and E. Osinga[4]

[1] Hamburger Sternwarte, University of Hamburg, Gojenbergsweg 112, 21029 Hamburg, Germany
e-mail: marco.simonte@hs.uni-hamburg.de
[2] Thüringer Landessternwarte, Sternwarte 5, 07778 Tautenburg, Germany
[3] Institute for Astronomy, University of Edinburgh, Royal Observatory, Blackford Hill, Edinburgh EH9 3HJ, UK
[4] Leiden Observatory, Leiden University, PO Box 9513, 2300 RA Leiden, The Netherlands

ABSTRACT

Aims. Previous studies reported an alignment of the major axes of radio galaxies on various angular scales. Here, we study the alignment of radio galaxies in the ELAIS-N1 Low Frequency ARray (LOFAR) deep field, which covers an area of 25 deg^2.
Methods. The low noise level of about 20 μJy beam^{-1} of the LOFAR deep field observations at 150 MHz enabled the identification of 447 extended (>30″) radio galaxies for which we measured the position angle of the major axis. We find that 95% of these sources have either photometric or spectroscopic redshifts, which we then used for a three-dimensional (3D) analysis.
Results. We show the distribution of the position angles of radio galaxies in the ELAIS-N1 field and the results of multiple statistical tests carried out to decipher whether the radio galaxies are randomly oriented. We find that the distribution of position angles is consistent with being uniform. Two peaks around position angles of 50 and 140 deg are spurious and are not caused by an alignment, as shown by a 3D analysis. In conclusion, our results do not support a 2D or 3D alignment of radio galaxies on scales of smaller than ~4 deg.

Key words. galaxies: active – galaxies: jets – radio continuum: galaxies

1. Introduction

The cosmological principle is an assumption in modern cosmology that states that the Universe is (statistically) isotropic and homogeneous on suitably large scales ($\gtrsim$100 Mpc). Multiple observations have been carried out in order to investigate the degree of anisotropy in the cosmic microwave background (Bennett et al. 1996; Hansen et al. 2004; Planck Collaboration XVI 2016; Planck Collaboration VII 2020) confirming the principle of homogeneity and isotropy of the Universe. However, several authors have reported an intriguing alignment of the linear polarisation of quasars (Stockman et al. 1979; Hutsemekers 1998; Hutsemékers & Lamy 2001; Jain et al. 2004; Cabanac et al. 2005; Pelgrims & Cudell 2014; Slagter & Miedema 2021; Friday et al. 2022). Interestingly, they found an alignment mainly occurring in groups of 10–30 objects and potentially on gigaparsec (Gpc) scales.

Some other studies focused on the alignment of radio galaxy jets (e.g., Sanders 1984; Kapahi et al. 1985; West 1991; Joshi et al. 2007; Tiwari & Jain 2013), and some of their findings support a possible departure from the cosmological principle. Taylor & Jagannathan (2016) studied the spatial distributions of the major-axis position angle of radio galaxies in the ELAIS-N1 Giant Metrewave Radio Telescope (GMRT, Ananthakrishnan 1995) deep field. These authors claimed the existence of a 2D alignment around $PA \sim 140°$ over an area of $\sim$ 1.7 deg^2.

However, without redshift information for the host galaxies, they were not able to perform a 3D analysis. The first attempts to detect an alignment on larger scales were made by Contigiani et al. (2017) and Panwar & Prabhakar (2020) who used catalogue data from the Faint Images of the Radio Sky at Twenty-centimetres (FIRST, Becker et al. 1995; Helfand et al. 2015) and the TIFR GMRT Sky Survey (TGSS, Intema et al. 2017). Contigiani et al. (2017) and Panwar & Prabhakar (2020) detected a signal over a scale of smaller than 2°, but did not find strong evidence for a 3D alignment. For the first time, Blinov et al. (2020) explored the alignment of parsec-scale jets, finding that their radio sources do not show any global alignment. However, Mandarakas et al. (2021), with a similar but larger sample, detected a strong signal of an alignment of parsec-scale jets in multiple regions of the sky. Nevertheless, the redshift distribution of their sources spans a wide range, $0 < z \lesssim 1.5$. Most recently, Osinga et al. (2020) searched for alignment using 7555 extended sources from the first data release of the Low Frequency ARray Two metre Sky Survey (LoTSS, Shimwell et al. 2019). However, despite their use of host redshifts, Osinga et al. (2020) were only able to detect a 2D alignment of the position angles of the radio galaxies over a scale of 5° and were unable to exclude the possibility that the signal arises from systematic effects.

Although multiple studies have now presented evidence for a 2D or 3D alignment, an explanation for such a phenomenon is lacking. West (1991), Hutsemékers et al. (2014) and Pelgrims & Hutsemékers (2016) found an alignment between the radio and optical emissions from active galactic nuclei (AGN) and the surrounding large-scale structure. Moreover, Malarecki et al. (2013, 2015) showed that giant radio galaxies (Willis et al. 1974) have a tendency to grow in a direction

perpendicular to the major axes of galaxy overdensities. However, the connection between the orientation of radio galaxy jets and the large-scale structure is unclear.

In this paper, we revisit the alignment of the jets of radio galaxies in the ELAIS-N1 field. We make use of photometric redshifts of the host galaxies to perform a 3D analysis.

The layout of this paper is as follows: In Sect. 2 we explain how we built our catalogue of extended radio galaxies (ERGs) and how we measured their orientation. In Sect. 3 we present the results of our 2D and 3D analyses. In Sect. 4, we discuss our results in the context of theoretical and observational work on the orientation of radio galaxies and provide a summary.

Throughout this work we adopt a flat ΛCDM cosmology with $H_0 = 70 \, \text{km s}^{-1} \, \text{Mpc}^{-1}$, $\Omega_{\text{m}} = 0.3$, and $\Omega_{\Lambda} = 0.7$.

2. Methods

We inspected the ELAIS-N1 LOw-Frequency ARray (LOFAR, van Haarlem et al. 2013) deep field (Sabater et al. 2021). With an effective observing time of 163.7 h, it reaches a root mean square noise level at 150 MHz lower than 30 μJy beam^{-1} across the inner 10 deg^2 and below 20 μJy beam^{-1} in the very centre. The ELAIS-N1 LOFAR Deep Field (ELDF) is centred on 16h11m00s + 55°00′00″(J2000) and covers an area of about 25 deg^2. The 6″ resolution of the radio image ensures a robust classification of the sources and, most importantly, the identification of the hosts and radio features such as jets and hotspots.

2.1. The sample of extended radio galaxies

We searched for all the ERGs with a largest angular size (LAS) of greater than ~30″ within an area of ~25 deg^2. We measured the LAS as the distance between the opposite ends of the ERGs. However, this method can overestimate the size of the Fanaroff-Riley type II (FRII, Fanaroff & Riley 1974) as mentioned by Kuźmicz & Jamrozy (2021). For ERGs of this kind, we therefore measured the LAS as the distance between the two hotspots, whenever identified on the VLA Sky Survey images (Lacy et al. 2020). The radio position angles (RPAs) were manually measured (using Aladin[1], Bonnarel et al. 2000) in the range of [0, 180) degrees as the angle between the major axis and the local meridian of the sources from N through E. For straight (or only slightly bent) FRI and FRII ERGs, the RPA is either that of the inner jets (FR I) or that of the direction connecting the two hotspots (FR II). In the case of bent sources (e.g., wide-angle-tailed RGs), measuring the RPA is less trivial. For such cases, we measured the RPA in the vicinity of the core where the jets are not usually bent yet and flagged them as uncertain measurements. We carefully avoided measuring the RPA of overlapping sources unless the morphology of the ERGs was very clear.

A large number of optical and infrared surveys, such as the Wide-Field Infrared Survey Explorer (WISE, Cutri et al. 2012, 2013; Schlafly et al. 2019; Marocco et al. 2021), the Sloan Digital Sky Survey (SDSS, York et al. 2000), the Legacy survey (Dey et al. 2019), and the Panoramic Survey Telescope and Rapid Response System (Pan-STARRS, Flewelling et al. 2020) enabled us to identify the host galaxies (see Kondapally et al. 2021; Andernach et al. 2021; Simonte et al. 2022, for further details of the host identification and radio-source classification). We looked for available spectroscopic (Ahumada et al. 2020) and photometric (Rowan-Robinson et al. 2013; Bilicki et al. 2014, 2016;

Beck et al. 2016, 2021; Zhou et al. 2021; Duncan et al. 2021; Wen & Han 2021; Duncan 2022) redshifts in multiple catalogues. If multiple photometric redshifts were available for a single source, we computed their mean and error by taking the standard deviation of the various redshifts. For spectroscopic redshifts, we do not report errors because they are generally more accurate (typical errors are usually around 0.00015) than the precision we can achieve on the linear size given our errors in measuring the angular size. There is no available redshift estimate for 15 host galaxies; these sources are either optically very faint or are only detected in the infrared. The deepest full-sky catalogue is the Zhou et al. (2021) DESI DR9 photometric redshift catalogue (a deeper catalogue from Duncan et al. (2021) exists over the inner 7 deg^2 of the ELAIS-N1 field). In Zhou et al. (2021), the faintest galaxies have a maximum redshift of around 1.3. We therefore assumed a redshift in the range of 1.1–1.5 for those host galaxies without redshift listed in the literature. This assumption will not affect our analysis as we used only those sources with a redshift reported in the literature for the 3D analysis.

We find 447 ERGs for which we provide a redshift, LAS, largest linear size (LLS), and RPA. We show some of our ERGs in Table A.1 and the full list will be made available at the CDS and through the VizieR service[2] (Ochsenbein et al. 2000). To test the alignment in the region inspected by Taylor & Jagannathan (2016), we located all the sources that these authors used in their analysis (their Fig. 2) and measured their RPAs. Some of these RGs have an angular size of smaller than 30″. The resolution of 6″ of the LOFAR images does not enable reliable measurement of the RPA of the smallest sources and we flagged these measurements as uncertain. We had to discard 9 RGs used by Taylor & Jagannathan (2016) as 8 of them are separate sources and one is a spiral galaxy (see Appendix A). However, we were able to identify a further 24 ERGs using the LOFAR data within the sky area studied by these latter authors and added these to our sample. Table 1 compares our sample with previous lists of RGs used for the RPA analysis. In this work, we analysed a field that is approximately ten times larger than that of Taylor & Jagannathan (2016), but much smaller than those used by Contigiani et al. (2017), Panwar & Prabhakar (2020), and Osinga et al. (2020). Nevertheless, our sample has the largest RG sky density in the central region $(241.5° < \text{RA} < 243.75°, 53.9° < \text{Dec} < 55.2°)$, which is reported in the last row of Table 1, while the second-to-last row shows the RG sky density considering the full ELDF.

2.2. Statistical tests

We performed multiple tests to assess the (non-)uniformity of the RPA distribution. Different methods have been used in past analyses to study the distribution of the orientation of RGs. We use five different tests for (non-)uniformity of angles:

1. The Kolmogorov-Smirnov (KS) test compares the underlying distribution of the sample of the RPA against a given distribution, which in our case is a uniform distribution. The null hypothesis is that the two distributions are identical and the closer the p-value is to zero the more confident we are in rejecting the null hypothesis. A common threshold used to reject the null hypothesis of the two distributions being drawn from the same population is a p-value $p < 0.05$, which means that there is only a 5% chance that the two samples are in fact drawn from the same population.

---

[1] https://aladin.cds.unistra.fr

[2] https://vizier.cds.unistra.fr

Table 1. Comparison between our catalogue and previous samples.

(1) Survey	(2) Freq. (GHz)	(3) RMS (mJy/b)	(4) N of (RGs)	(5) RGs density (deg^{-2})
Taylor [1]	0.61	0.01	65	38.2
FIRST [2]	1.4	0.15	30059	4.3
FIRST [3]	1.4	0.15	18775	1.9
LoTSS [4]	0.15	0.07	7555	17.8
ELDF [5]	0.15	0.03	447	17.9
ELDF-C [6]	0.15	0.02	78	45.9

References. [1] Taylor & Jagannathan (2016), [2] Contigiani et al. (2017), [3] Panwar & Prabhakar (2020), [4] Osinga et al. (2020), [5,6] this work: ELDF-C refers to the central region of the ELDF ($241.5° <$ RA $< 243.75°, 53.9° <$ Dec $< 55.2°$).

2. Pearson's χ^2 test for uniformity tests the null hypothesis that the frequency distribution of certain events observed in a sample is consistent with a particular theoretical distribution (in our case a uniform one). As with the KS test, the smaller the p-value the more likely it is that the two distributions are different. This test is performed with binned data, and in our case we used 18 bins of 10° in width.

3. Our set of RPAs belongs to the category of circular data (Fisher 1993), which are fundamentally different from linear data due to their periodic nature. The Rayleigh test (Mardia & Jupp 2000) assesses the uniformity of circular data. To this end, this test compares the test statistic of the unit vector resulting from the sum of all the vectors pointing towards the different angles of the sample, with the same statistics estimated from a uniformly distributed sample. The null hypothesis of such test is that the data are uniformly distributed over the circle. The test statistic is the mean resultant length of the unit vector and is defined as

$$\bar{R} = \frac{1}{n}\left[\left(\sum_{i=1}^{n}\cos\theta_i\right)^2 + \left(\sum_{i=1}^{n}\sin\theta_i\right)^2\right]^{1/2},\qquad(1)$$

where n is the size of the sample and the angles θ_i are the RPAs multiplied by two (because these are orientations (axial vectors) in the range [0°, 180°] while the Rayleigh test is performed on the range [0°, 360°]). $\bar{R}$ can range from 0 to 1. This statistic is zero for a uniform distribution, and therefore it is reasonable to reject uniformity when R is large. It is worth mentioning that this test is not sensitive to non-uniform distributions that have $\bar{R} = 0$. An example is a bimodal distribution with two peaks that are 180° apart as every vector pointing towards a certain direction is cancelled by a vector pointing along the opposite direction. This issue can mildly affect our analysis because the major peaks in our distributions of the RPAs are 180° apart once the RPAs are multiplied by two (see Sect. 3 below).

4. The semi-variance (Cressie 1993) is a statistical tool used in spatial analysis to measure the dispersion of a certain variable on different scales. It is defined as follows:

$$\gamma(d) = \frac{1}{2m(d)}\sum_{i=1}^{m(d)}[s(x_i) - s(x_i + d)]^2,\qquad(2)$$

where $m(d)$ is the number of pairs separated by a (angular) distance in the range $[d, d + \delta d]$ (we used $\delta d = 0.2°$) and s is the variable measured at the vector location x_i and in our case is the

RPA of the ERGs. The semi-variance is constant over all angular scales when the distribution of the variable s is uniform. A value for the semi-variance of smaller than what is predicted by a uniform distribution at a certain scale indicates an alignment of the ERGs. On the other hand, a larger semi-variance suggests a larger dispersion than expected from a random distribution, indicating that no alignment is present on that scale. We performed a simple Monte-Carlo simulation to infer the value of the semi-variance of randomly distributed ERGs on different angular scales. We generated 447 (which is the size of our sample) random angles uniformly distributed in the range [0, 180), which have the same spatial distribution as the ERGs in our sample and we computed the semi-variance on different angular scales. We repeated the operation 10 000 times and then averaged the semi-variance values on the different scales. We folded the data in circularity to take into account the periodicity of the RPAs. On every scale, we obtained a constant semi-variance of 0.82, which is consistent with the result from Taylor & Jagannathan (2016). The error on the semi-variance, $\sigma_{\rm SM}$ was estimated by calculating the standard deviation of the 10 000 values on each angular scale.

5. Finally, we probed the alignment of the ERGs at different angular scales using the dispersion measure analysis (Jain et al. 2004). The dispersion measure is defined as the inner product between a certain position angle θ and the RPAs, θ_k, of the n closest sources to a certain ith ERG (including the source itself) and it is an indication of the alignment of the ERGs. Following Jain et al. (2004), Contigiani et al. (2017), and Osinga et al. (2020), it can be shown that the maximum dispersion measure around the source i is

$$D_{i,n}|_{\max} = \frac{1}{n}\left[\left(\sum_{k=1}^{n}\cos(\theta_k)\right)^2 + \left(\sum_{k=1}^{n}\sin(\theta_k)\right)^2\right]^{1/2}.\qquad(3)$$

The closer $D_{i,n}|_{\max}$ is to 1, the more aligned the n galaxies are. The statistic, S_n used to test the (non-)uniformity of the distribution of the RPAs is the average of the $D_{i,n}|_{\max}$ calculated for each source of the sample. This statistic computed from our dataset is compared to the same statistics coming from Monte-Carlo-simulated samples, $S_{n,\rm MC}$. To compute $S_{n,\rm MC}$ we generated 447 randomly oriented ERGs with the same spatial distribution as our sources and followed the formalism described in Jain et al. (2004), Contigiani et al. (2017) and Osinga et al. (2020). We repeated the calculation of $S_{n,\rm MC}$ 10 000 times and estimated the average, $\langle S_{n,\rm MC}\rangle$, and the error, $\sigma_{n,\rm MC}$, as the standard deviation of 10 000 generated statistics. The significance level for rejecting the null hypothesis that a sample of ERGs is randomly oriented is found through a one-tailed significance test, expressed as:

$$SL = 1 - \Phi\left(\frac{S_n - \langle S_{n,\rm MC}\rangle}{\sigma_{n,\rm MC}}\right),\qquad(4)$$

where Φ is the cumulative normal distribution function. The closer the significance level is to zero the more confident we are in rejecting the hypothesis of uniformity. As the number of nearest neighbours can be translated to an angular scale extending to the nth nearest neighbour, we can probe multiple angular scales by varying n. To do so, we calculated the maximum angular distance between the relevant ERG and the nth closest neighbour and took the median value among the 447 sources. The same analysis can be implemented considering the 3D position of the ERGs to test whether a 3D alignment is present between sources that are physically close to each other. We approximated the redshift of the source with the average redshift estimated for
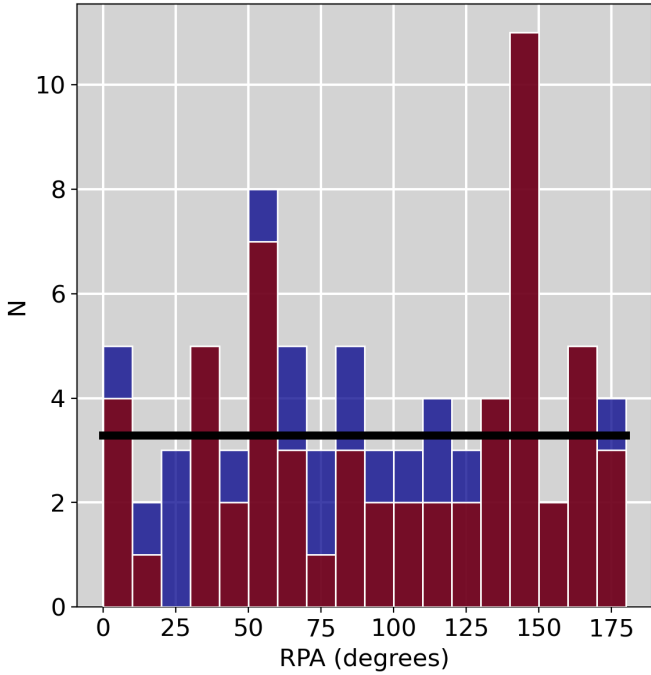
Fig. 1. Distribution of the RPAs of the 78 ERGs (blue histogram) that we found in the inner region of the ELDF and of the 59 certain sources (red histogram). The black line shows the expected number of objects per bin for a uniform distribution of 78 ERGs.

each ERG without taking into account the error and we did not include those sources without a redshift value reported in the literature. The uncertainties of some redshift estimations could mildly affect the analysis: in fact, while ERGs with $z < 1$ have a redshift error of about 0.05, for more distant sources, which represent 30% of our sample, the error increases to 0.2. We then converted the redshift to comoving distance and measured the 3D comoving distance between all the ERGs in our sample.

Moreover, Jain et al. (2004) verified that the variance of the statistic S_n is inversely proportional to the size of the sample which means that, compared to Contigiani et al. (2017) and Osinga et al. (2020), who used much larger samples, we are more affected by the shot noise.

3. Results

In this section, we present the distribution of the RPAs in the ELAIS-N1 field. We initially focus on the inner region studied by Taylor & Jagannathan (2016) and then expand the analysis to the entire ELDF.

3.1. Alignment in the central part of ELAIS-N1

Here, we look at the distribution of the RPAs in the inner $\sim 1.7\,\mathrm{deg}^2$ of the ELAIS-N1 field ($241.5 < \mathrm{RA} < 243.75$, $53.9 < \mathrm{Dec} < 55.2$), where Taylor & Jagannathan (2016) found a statistically significant alignment of radio galaxies. We recall that 9 of the radio sources they used in their analysis are not genuine radio galaxies and we were able to add a further 24 ERGs using LOFAR data. Thus, the sample for such an analysis consists of 78 ERGs, of which 19 are flagged as uncertain RPA measurements. We show the distribution of the RPAs in the inner region of the ELAIS-N1 field in Fig. 1. The blue histogram shows the distribution of the total sample of RPAs in this region, while the

red histogram shows the same but with the uncertain measurements excluded. The figure clearly shows a peak at RPAs around 140°, which is in agreement with Taylor & Jagannathan (2016). We then carried out the statistical tests explained in Sect. 2.2 and found a p-value of 0.66 and 0.31 for the KS test and the χ^2 test, respectively. The latter test is valid for large samples and it is customary to recommend in applications of the test that the smallest expected number should be 5 in any one bin (Cochran 1952). We performed the test using 13 bins, each with a width of 15°, which lead to an expected value of about 6.5 elements per bin. The resulting p-value is 0.23 in this case. Concerning the Rayleigh test, we find a mean resultant length of $\bar{R} = 0.009$ which results in a p-value = 0.96. Therefore, even though the distribution shows a clear peak, we cannot reject the hypothesis of uniformity of the RPAs in this region. Moreover, the analysis involving the semi-variance (Fig. 2) shows that there is no correlation between the RPAs of the ERGs located at different positions on the sky at any angular scale. In Fig. 2, the blue line and points are the values estimated using randomly generated data that have the same spatial distribution as the 78 ERGs in the inner region of the ELAIS-N1 field, while the orange points are the result of the analysis performed on our dataset.

We did not perform an analysis based on the dispersion measure (i.e. method 5 listed in Sect. 2.2) because of the smaller number of ERGs when restricting the study to the inner region of the field. With a sample of only 78 objects, we are certainly dominated by the shot noise (Jain et al. 2004), which would cancel out any signal unless the alignment is very strong, which does not seem to be the case here.

We performed the statistical tests on the sample of 59 ERGs for which we could measure a reliable RPA as well. We obtained p-values of 0.10, 0.01 and 0.46 for the KS, χ^2, and Rayleigh test, respectively. The result of the χ^2 test holds when considering bins with a width of 15°. Nevertheless, this is the only test that suggests an alignment of the ERGs in the inner region; we reiterate that the semi-variance test applied to this smaller sample cannot reject the hypothesis of a uniform distribution.

The sensitivity of the LOFAR ($20\,\mu\mathrm{Jy\,beam^{-1}}$) and GMRT ($10\,\mu\mathrm{Jy\,beam^{-1}}$) ELAIS-N1 deep field observations are quite similar, but the four-times-lower frequency of LOFAR makes an RG with a typical spectral index of -0.8 about three times brighter at 144 MHz compared to 610 MHz. Moreover, the availability of deeper infrared source catalogues, such as CatWISE (Marocco et al. 2021) and unWISE (Schlafly et al. 2019), enables the identification of more distant galaxies, which may emit in the radio band as point-like sources. Such contamination, if superimposed on the emission of an ERG, may slightly change the morphology of the latter and lead to an erroneous RPA measurement.

In order to attempt to reproduce the Taylor & Jagannathan (2016) results, we extracted the positions, sizes and RPAs of the RGs from their Fig. 2 as follows: the end points of all vectors were digitised with the g3data software, and saved as RA, DEC in degrees. We then reviewed the RPA measurements and were able to closely match the histogram shown in their Fig. 3. We ran our first four statistical tests on the recovered data, but found that none of them is able to reject the hypothesis of uniformity. In particular, for the Rayleigh test, we obtained a mean resultant length of 0.09 from our analysis of these data, which is highly discrepant with the value of 0.68 derived by Taylor & Jagannathan (2016) that led them to claim a non-uniformity of RPAs. The origin of this difference is uncertain, although we note that if we do not multiply the RPAs by a factor of two (a step that is required, because the test assesses uniformity over a circle and
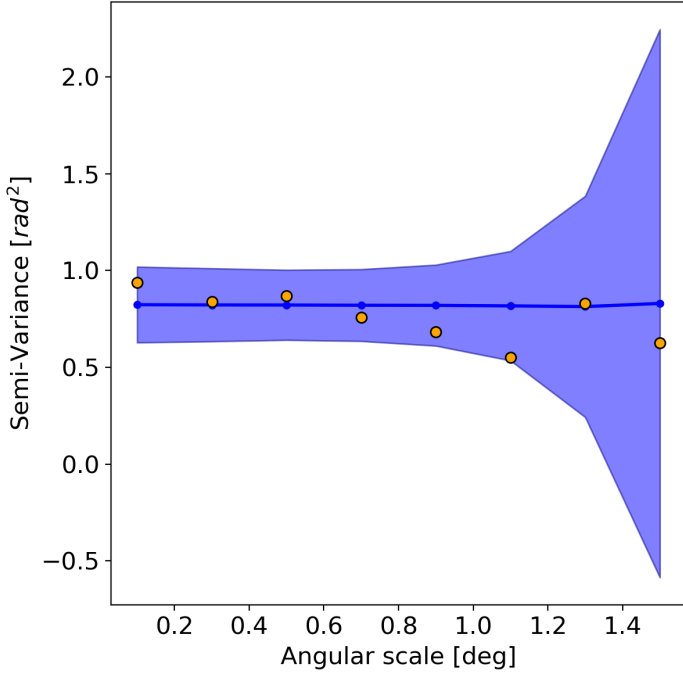
Fig. 2. Estimate of the semi-variance on different angular scales in the inner region of the ELAIS-N1 field. The blue line and points are the semi-variance values obtained for randomly generated position angles with the same spatial distribution of the 78 ERGs. The shadowed region represents the $2\sigma_{SM}$ values. The orange points are estimated from our dataset.

Fig. 3. Distribution of the RPAs of the 447 ERGs we find in the ELDF (red histograms) and of the 377 certain sources (red histogram). The black line shows the expected number of objects per bin for a uniform distribution considering the total sample.

the RPAs are distributed over $[0, 180)$, we obtain an erroneous mean resultant length of 0.64, which is much closer to the value quoted by Taylor & Jagannathan (2016).

3.2. Alignment in the entire ELAIS-N1 field

We show the distribution of the RPAs of the radio galaxies in the ELDF in Fig. 3. The blue histogram represents the total sample, while the red histogram shows the distribution for the 377 certain sources, that is, those ERGs that do not show a complex morphology and for which we were able to accurately measure the RPA. The black line denotes the expected number of objects per bin if the distribution were uniform. We subsequently performed the same statistical tests considering the total sample. The results, with p-values equal to 0.71, 0.33, and 0.88 for the KS test, χ^2 test, and Rayleigh test, respectively, suggest that the uniformity holds when including the entire field as well. These results are also confirmed by the analysis of the semi-variance. We measured the semi-variance in our sample, shown by the orange points in Fig. 4. The blue line and points are the semi-variance values estimated from randomly generated data and the shadowed region represents the $2\sigma_{SM}$ values. The larger uncertainties on the largest scale are due to poor statistics, because not many pairs are separated by such large distances. Overall, there is no clear evidence for a convincing signal in favour of an alignment as the orange points are always consistent with 0.82 within the error.

Finally, we show the results of the 2D (black line) and 3D (blue line) dispersion measure tests in Fig. 5. The significance level, SL, is plotted as a function of the number of nearest neighbours, n, and angular scale in degrees. Following previous studies (e.g. Contigiani et al. 2017), a commonly used criterion for the presence of an alignment signal is $SL < 0.03$
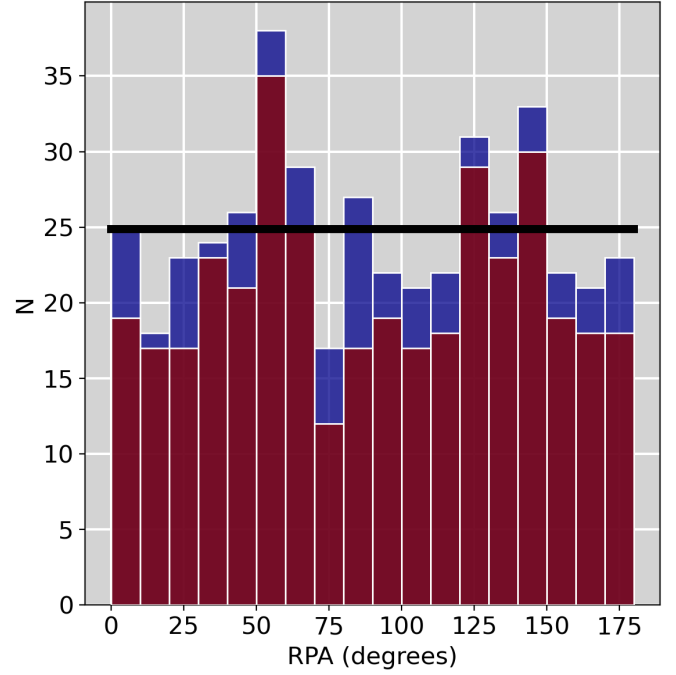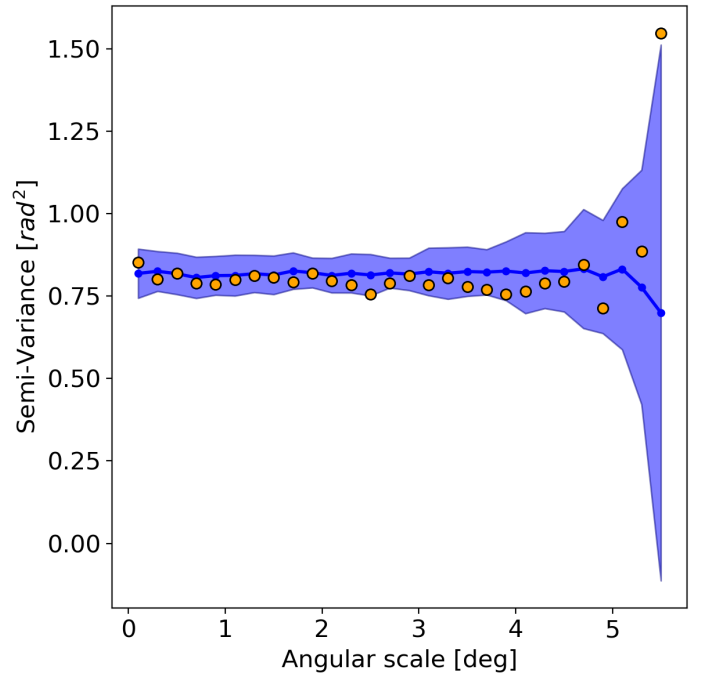

Fig. 4. Estimate of the semi-variance on different angular scales. The blue line and points highlight the constant value of the semi-variance for randomly generated position angles with the same spatial distribution of the 447 ERGs in our sample. The shadowed region represents the $2\sigma_{SM}$ values. The orange points are the semi-variance values of our sample.

($\text{Log}(SL) < -1.5$.). As mentioned in Sect. 2.2, our analysis is more affected by the shot noise because of the comparatively small size of our sample. However, a minimum significance level of about 0.2 in Fig. 5 suggests there is no evident signal, either in the 2D or in the 3D analysis, at any scale.
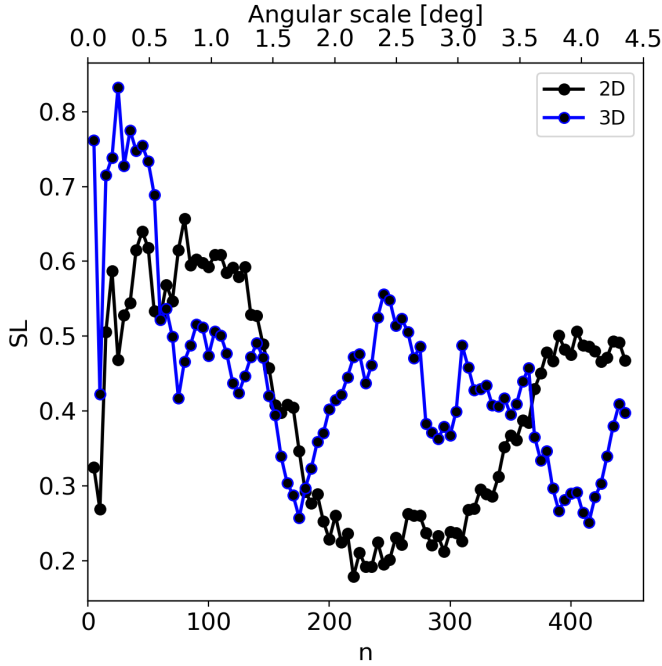
Fig. 5. Significance level of the dispersion measure test (SL) as a function of the nearest neighbours (*n*, lower abscissa) and angular scale in degrees (upper abscissa). The black line shows the results of the 2D analysis while the 3D analysis is shown with the blue line. Such a large SL ($\gg$0.03) shows that no alignment is present in the ELAIS-N1 field at any scale in our analysis.

These results also hold when considering only the ERGs with reliable RPA measurement.

Even though the tests suggest that radio galaxies are randomly oriented, two conspicuous peaks are visible on an RPA range: one between 50°−60° and another between 140°−150° (the latter was seen by Taylor & Jagannathan 2016 as well). The Poisson distribution gives the probability of a given number of observations occurring in a fixed interval of PAs, where the rate of occurrence of these observations is constant and known. This rate is obtained from the uniform distribution. Therefore, using such a distribution, we find that the two peaks are ∼2.5σ (for RPAs between 50° and 60°) and ∼1.5σ (for RPA between 140° and 150°) above the average. Figure 6 shows the spatial and redshift distributions of the ERGs with an orientation of between 50° and 60° (upper panel) and between 140° and 150° (lower panel). We selected the ERGs up to redshift 1.5 because the majority of ERGs at larger redshifts either do not have a redshift estimate in the literature or have very large errors. The black rectangles highlight the region inspected by Taylor & Jagannathan (2016). In both cases, there is no 3D alignment of ERGs as the redshifts span the range of $0.1 \lesssim z \lesssim 1.5$.

4. Discussion and summary

The tidal torque theory predicts that the angular momentum of the dark matter proto-halos is acquired during their formation which occurs along the entire evolution of the large-scale structure of the Universe (Peebles 1969; Doroshkevich 1970; White 1984; Porciani et al. 2002; Schäfer 2009). As a result, an alignment between optical galaxies and the large-scale structure (e.g., filaments and sheets) is expected (Hu et al. 2006; Joachimi et al. 2015; Kirk et al. 2015). In a first attempt to study this alignment, Hawley & Peebles (1975) found a small departure from
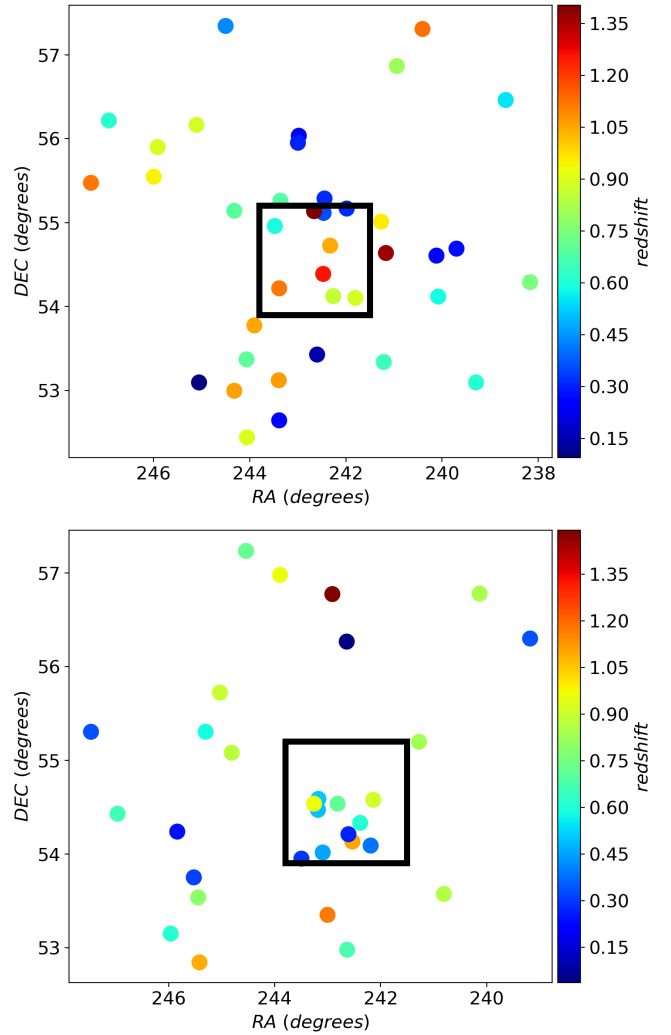

Fig. 6. Spatial distribution of 39 ERGs with RPA between 50° and 60° (upper panel) and 31 ERGs with RPA in the range 140°−150°. The colour bar shows the redshifts of the ERGs. The analysis was restricted to $z \leq 1.5$. The black box represents the field of Taylor & Jagannathan (2016).

isotropy in the distribution of the orientation angle, which is measured as the angle between the major axis of the galaxy and the local meridian. Lee (2004) argued that the observed large-scale coherence in the orientation of nearby spiral galaxies found by Navarro et al. (2004) can be fully explained by the tidal torque theory. Others have tried to look at a possible alignment of galaxies and most authors found that the minor axes of early-type galaxies are preferentially oriented perpendicular to the host filament (Tempel et al. 2013; Tempel & Libeskind 2013; Hirv et al. 2017), while late-type galaxies have spin axes parallel to the closest filament (Tempel et al. 2013; Tempel & Libeskind 2013; Hirv et al. 2017; Blue Bird et al. 2020; Kraljic et al. 2021; Tudorache et al. 2022). However, some conflicting results have been found (Jones et al. 2010; Zhang et al. 2015; Pahwa et al. 2016; Krolewski et al. 2019). Recently, Rodriguez et al. (2023), using the IllustrisTNG simulations (Nelson et al. 2019), found an alignment with the large-scale structure of red galaxies in the centres of galaxy clusters and groups. These authors then speculated that this anisotropy in the orientation of the central galaxies is the consequence of a concatenation of alignments. Starting from the alignment between the central galaxy and the host clus-

ter (Yuan & Wen 2022), eventually, the host halo aligns with the structures surrounding it.

Some work found that there is a mild preference for radio jets to align with the minor axis of the galaxy host (Kotanyi & Ekers 1979; Battye & Browne 2009; Kamali et al. 2019; Vazquez Najar & Andernach 2019). Assuming that the alignment between radio jets and optical galaxies is real, one could in principle look at the alignment between the radio galaxies and the large-scale structure (e.g. West 1991). Nevertheless, some opposing results regarding the orientations of radio jets have been found (Schmitt et al. 2002; Verdoes Kleijn & de Zeeuw 2005; Hopkins et al. 2012), casting doubts on this assumption.

In the present work, we revisited the alignment of radio jets in the ELAIS-N1 field. We inspected the LOFAR ELAIS-N1 deep field in which we identified the host galaxies of 447 ERGs whose radio emission extends over at least ~0.5′. We measured the RPA of the major radio axis (assuming it to be a tracer of the underlying radio jet direction) and studied its distribution using a number of statistical tests, none of which is able to reject the null hypothesis of uniform orientations. Similar results are obtained when restricting the analysis to the region inspected by Taylor & Jagannathan (2016). Only when restricting the sample to the 59 ERGs with a reliable RPA measurement in the inner region does the χ^2 test return a p-value = 0.01 (i.e. it suggests there is a 1% chance that the result is a statistical fluctuation). However, none of the other statistical tests on this sample are able to reject the hypothesis of uniformity of the RPA distribution. We recovered the data used by Taylor & Jagannathan (2016) in their analysis and show that, even with this sample, we cannot obtain the same results. Furthermore, we find that the redshifts of ERGs with orientations near the two peaks (around 50° and 140°) span a wide range, namely $0.1 \lesssim z \lesssim 1.5$, strongly arguing against the idea of a 3D alignment of radio galaxies. Other reports of a 3D alignment (e.g., Contigiani et al. 2017; Panwar & Prabhakar 2020) have not been statistically significant. However, several studies reported a 2D alignment (Contigiani et al. 2017; Panwar & Prabhakar 2020; Mandarakas et al. 2021) over angular scales similar to those that we studied. The maximum angular scale we were able to explore is ~4° (see Fig. 4), which is the scale over which Osinga et al. (2020) found a 2D alignment. The combination of the two results might suggest that the 2D alignment of radio galaxies may exist on scales larger than those probed by our analysis.

References

Ahumada, R., Allende Prieto, C., Almeida, A., et al. 2020, ApJS, 249, 3
Ananthakrishnan, S. 1995, J. Astrophys. Astron. Suppl., 16, 427
Andernach, H., Jiménez-Andrade, E. F., & Willis, A. G. 2021, Galaxies, 9, 99
Battye, R. A., & Browne, I. W. A. 2009, MNRAS, 399, 1888
Beck, R., Dobos, L., Budavári, T., Szalay, A. S., & Csabai, I. 2016, MNRAS, 460, 1371
Beck, R., Szapudi, I., Flewelling, H., et al. 2021, MNRAS, 500, 1633
Becker, R. H., White, R. L., & Helfand, D. J. 1995, ApJ, 450, 559
Bennett, C. L., Banday, A. J., Gorski, K. M., et al. 1996, ApJ, 464, L1
Bilicki, M., Jarrett, T. H., Peacock, J. A., Cluver, M. E., & Steward, L. 2014, ApJS, 210, 9
Bilicki, M., Peacock, J. A., Jarrett, T. H., et al. 2016, ApJS, 225, 5
Blinov, D., Casadio, C., Mandarakas, N., & Angelakis, E. 2020, A&A, 635, A102
Blue Bird, J., Davis, J., Luber, N., et al. 2020, MNRAS, 492, 153
Bonnarel, F., Fernique, P., Bienaymé, O., et al. 2000, A&AS, 143, 33
Cabanac, R. A., Hutsemékers, D., Sluse, D., & Lamy, H. 2005, in Astronomical Polarimetry: Current Status and Future Directions, eds. A. Adamson, C. Aspin, C. Davis, & T. Fujiyoshi, ASP Conf. Ser., 343, 498
Cochran, W. G. 1952, Ann. Math. Stat., 23, 315
Contigiani, O., de Gasperin, F., Miley, G. K., et al. 2017, MNRAS, 472, 636
Cressie, N. A. C. 1993, Statistics for Spatial Data (John Wiley & Sons)
Cutri, R. M., et al. 2012, VizieR Online Data Catalog: II/311
Cutri, R. M., Wright, E. L., Conrow, T., et al. 2013, Explanatory Supplement to the AllWISE Data Release Products
Dey, A., Schlegel, D. J., Lang, D., et al. 2019, AJ, 157, 168
Doroshkevich, A. G. 1970, Astrophysics, 6, 320
Duncan, K. J. 2022, MNRAS, 512, 3662
Duncan, K. J., Kondapally, R., Brown, M. J. I., et al. 2021, A&A, 648, A4
Fanaroff, B. L., & Riley, J. M. 1974, MNRAS, 167, 31P
Fisher, N. I. 1993, Statistical Analysis of Circular Data (Cambridge University Press)
Flewelling, H. A., Magnier, E. A., Chambers, K. C., et al. 2020, ApJS, 251, 7
Friday, T., Clowes, R. G., & Williger, G. M. 2022, MNRAS, 511, 4159
Hansen, F. K., Banday, A. J., & Górski, K. M. 2004, MNRAS, 354, 641
Hawley, D. L., & Peebles, P. J. E. 1975, AJ, 80, 477
Helfand, D. J., White, R. L., & Becker, R. H. 2015, ApJ, 801, 26
Hirv, A., Pelt, J., Saar, E., et al. 2017, A&A, 599, A31
Hopkins, P. F., Hernquist, L., Hayward, C. C., & Narayanan, D. 2012, MNRAS, 425, 1121
Hu, F. X., Wu, G. X., Song, G. X., Yuan, Q. R., & Okamura, S. 2006, Ap&SS, 302, 43
Hutsemekers, D. 1998, A&A, 332, 410
Hutsemékers, D., & Lamy, H. 2001, A&A, 367, 381
Hutsemékers, D., Braibant, L., Pelgrims, V., & Sluse, D. 2014, A&A, 572, A18
Intema, H. T., Jagannathan, P., Mooley, K. P., & Frail, D. A. 2017, A&A, 598, A78
Jain, P., Narain, G., & Sarala, S. 2004, MNRAS, 347, 394
Joachimi, B., Cacciato, M., Kitching, T. D., et al. 2015, Space Sci. Rev., 193, 1
Jones, B. J. T., van de Weygaert, R., & Aragón-Calvo, M. A. 2010, MNRAS, 408, 897
Joshi, S. A., Battye, R. A., Browne, I. W. A., et al. 2007, MNRAS, 380, 162
Kamali, F., Henkel, C., Koyama, S., et al. 2019, A&A, 624, A42
Kapahi, V. K., Subrahmanyan, R., & Singal, A. K. 1985, Nature, 313, 463
Kirk, D., Brown, M. L., Hoekstra, H., et al. 2015, Space Sci. Rev., 193, 139
Kondapally, R., Best, P. N., Hardcastle, M. J., et al. 2021, A&A, 648, A3
Kotanyi, C. G., & Ekers, R. D. 1979, A&A, 73, L1
Kraljic, K., Duckworth, C., Tojeiro, R., et al. 2021, MNRAS, 504, 4626
Krolewski, A., Ho, S., Chen, Y.-C., et al. 2019, ApJ, 876, 52
Kuźmicz, A., & Jamrozy, M. 2021, ApJS, 253, 25
Lacy, M., Baum, S. A., Chandler, C. J., et al. 2020, PASP, 132, 035001
Lee, J. 2004, ApJ, 614, L1
Malarecki, J. M., Staveley-Smith, L., Saripalli, L., et al. 2013, MNRAS, 432, 200

Malarecki, J. M., Jones, D. H., Saripalli, L., Staveley-Smith, L., & Subrahmanyan, R. 2015, MNRAS, 449, 955

Mandarakas, N., Blinov, D., Casadio, C., et al. 2021, A&A, 653, A123

Mardia, K. V., & Jupp, P. E. 2000, Directional Statistics (John Wiley & Sons)

Marocco, F., Eisenhardt, P. R. M., Fowler, J. W., et al. 2021, ApJS, 253, 8

Navarro, J. F., Abadi, M. G., & Steinmetz, M. 2004, ApJ, 613, L41

Nelson, D., Springel, V., Pillepich, A., et al. 2019, Comput. Astrophys. Cosmol., 6, 2

Ochsenbein, F., Bauer, P., & Marcout, J. 2000, A&AS, 143, 23

Osinga, E., Miley, G. K., van Weeren, R. J., et al. 2020, A&A, 642, A70

Pahwa, I., Libeskind, N. I., Tempel, E., et al. 2016, MNRAS, 457, 695

Panwar, M., Prabhakar, Sandhu, & P. K., Wadadekar, Y., & Jain, P., 2020, MNRAS, 499, 1226

Peebles, P. J. E. 1969, ApJ, 155, 393

Pelgrims, V., & Cudell, J. R. 2014, MNRAS, 442, 1239

Pelgrims, V., & Hutsemékers, D. 2016, A&A, 590, A53

Planck Collaboration VII. 2020, A&A, 641, A7

Planck Collaboration XVI. 2016, A&A, 594, A16

Porciani, C., Dekel, A., & Hoffman, Y. 2002, MNRAS, 332, 339

Rodriguez, F., Merchán, M., Artale, M. C., & Andrews, M. 2023, MNRAS, 521, 5483

Rowan-Robinson, M., Gonzalez-Solares, E., Vaccari, M., & Marchetti, L. 2013, MNRAS, 428, 1958

Sabater, J., Best, P. N., Tasse, C., et al. 2021, A&A, 648, A2

Sanders, R. H. 1984, Nature, 309, 35

Schäfer, B. M. 2009, Int. Jo. Mod. Phys. D, 18, 173

Schlafly, E. F., Meisner, A. M., & Green, G. M. 2019, ApJS, 240, 30

Schmitt, H. R., Pringle, J. E., Clarke, C. J., & Kinney, A. L. 2002, ApJ, 575, 150

Shimwell, T. W., Tasse, C., Hardcastle, M. J., et al. 2019, A&A, 622, A1

Simonte, M., Andernach, H., Brüggen, M., et al. 2022, MNRAS, 515, 2032

Slagter, R. J., & Miedema, P. G. 2021, MNRAS, 501, 3054

Stockman, H. S., Angel, J. R. P., & Miley, G. K. 1979, ApJ, 227, L55

Taylor, A. R., & Jagannathan, P. 2016, MNRAS, 459, L36

Tempel, E., & Libeskind, N. I. 2013, ApJ, 775, L42

Tempel, E., Stoica, R. S., & Saar, E. 2013, MNRAS, 428, 1827

Tiwari, P., & Jain, P. 2013, Int. J. Mod. Phys D, 22, 1350089

Tudorache, M. N., Jarvis, M. J., Heywood, I., et al. 2022, MNRAS, 513, 2168

van Haarlem, M. P., Wise, M. W., Gunst, A. W., et al. 2013, A&A, 556, A2

Vazquez Najar, L. A., & Andernach, H. 2019, ArXiv e-prints [arXiv:1908.09989]

Verdoes Kleijn, G. A., & de Zeeuw, P. T. 2005, A&A, 435, 43

Wen, Z. L., & Han, J. L. 2021, MNRAS, 500, 1003

West, M. J. 1991, ApJ, 379, 19

White, S. D. M. 1984, ApJ, 286, 38

Willis, A. G., Strom, R. G., & Wilson, A. S. 1974, Nature, 250, 625

York, D. G., Adelman, J., Anderson, John E., J., , et al. 2000, AJ, 120, 1579

Yuan, Z. S., & Wen, Z. L. 2022, MNRAS, 516, 3159

Zhang, Y., Yang, X., Wang, H., et al. 2015, ApJ, 798, 17

Zhou, R., Newman, J. A., Mao, Y.-Y., et al. 2021, MNRAS, 501, 3309

Appendix A: Notes on discarded sources

J1609+5452 ($RA = 242.4899, DEC = 54.8794$). The radio emission coming from the two hotspots of this FRII candidate is the result of two separate point-like radio sources, hosted by SDSS J160958.85+545249.4 and CWISE J160956.26+545243.4.

J1609+5500 ($RA = 242.4858, DEC = 55.0000$) is actually two separate sources. The source to the NE is likely an RG itself (which we did not include in our sample) with an uncertain host galaxy. We propose CWISE J160959.21+550019.8 as the host candidate, even though the radio morphology makes this claim uncertain. On the other hand, the SW source is a clear wide-angle tailed (WAT) RG with host galaxy SDSS J160952.46+545937.9.

J1610+5416 ($RA = 242.5074, DEC = 54.2767$) might be a genuine RG with host SDSS J161002.72+541640.0. However, the radio morphology is very unclear and we consider the RPA measurement of this source to be very uncertain. Therefore, following the criteria applied during our inspection, we discarded this source.

J1610+5506 ($RA = 242.5574, DEC = 55.1125$) is a candidate RG whose radio emission is the result of at least two separate sources, hosted by SDSS J161013.41+550649.9 and SDSS J161014.30+550638.3.

J1612+5358 ($RA = 243.1542, DEC = 53.9686$) is the spiral galaxy SDSS J161236.98+535807.2. Thus, the RPA of the radio source is just the major axis of the galaxy and not that of any jets.

J1613+5411 ($RA = 243.3983, DEC = 54.1908$) is likely the combination of two different radio emissions. Part of the emission comes from the radio lobe of J1613+5412 an ERG (with host CWISE J161336.25+541258.4) that is included in our sample and whose RPA measurement is reliable. Moreover, there might be a contribution coming from the host galaxy SDSS J161334.98+541112.0 for which a reliable RPA measurement is not possible.

J1613+5414a ($RA = 243.4417, DEC = 54.2347$) is the NE lobe of another ERG (host galaxy CWISE J161334.24+541304.3) that we have in our sample and was used for the analysis. Again, there might be a contribution from another point-like source with host galaxy SDSS J161347.93+541405.6.

J1613+5414b ($RA = 243.3708, DEC = 54.2489$) is likely the result of the emission of two separate sources: DESI J243.3650+54.2490 and CWISE J161329.52+541454.7.

J1613+5415 ($RA = 243.4104, DEC = 54.2514$) is the N lobe of J1613+5412.

Table A.1. First 50 rows of the ERGs catalogue used for our analysis.

(1) Name	(2) RA$_J$ °	(3) Dec$_J$ °	(4) LAS (')	(5) RPA °	(6) FR type	(7) z	(8) Δz	(9) ztype	(10) Hostname	(11) type	(12) mag (mag)	(13) LLS (Mpc)
J1552+5540	238.1360	55.6731	0.50	10	II	1.50		e	CWISE J155232.64+554023.1	Qc	18.60W1	0.25
J1552+5417	238.1721	54.2920	0.68	50	II	0.74	0.06	p	SDSS J155241.30+541731.3	G	21.25r'	0.30
J1553+5454	238.2511	54.8994	1.23	30	II	0.97	0.23	p	DESI J238.2511+54.8994	Qc	23.67r	0.59
J1553+5516	238.3149	55.2773	0.45	155	II	0.88	0.04	p	DESI J238.3149+55.2773	G	23.11r	0.21
J1554+5506C	238.5454	55.1050	1.31	67	II	0.720		s	SDSS J155410.89+550617.9	G	22.11r'	0.57
J1554+5438	238.5471	54.6374	0.93	44	I/II	0.925		s	SDSS J155411.32+543814.8	G	21.09r'	0.44
J1554+5334	238.6527	53.5750	2.55	25	II	0.761		s	SDSS J155436.64+533430.0	G	21.61r'	1.13
J1554+5344	238.6665	53.7407	1.08	84	II	0.74	0.04	p	SDSS J155439.96+534426.5	G	22.07r'	0.47
J1554+5628	238.6835	56.4664	0.72	55	II	0.554		s	SDSS J155444.03+562758.9	G	20.85r'	0.28
J1556+5539	239.0106	55.6599	2.25	87	II	0.31	0.04	p	SDSS J155602.54+553935.6	G	18.80r'	0.62
J1556+5348	239.0622	53.8046	0.58	10	II	0.98	0.11	p	DESI J239.0622+53.8046	G	23.12r	0.28
J1556+5559	239.0914	55.9918	0.55	73	II	0.97	0.14	p	SDSS J155621.93+555930.5	G	22.55r'	0.26
J1556+5627	239.1139	56.4524	0.63	33	II	0.75	0.02	p	SDSS J155627.34+562708.8	G	21.04r'	0.28
J1556+5538	239.1143	55.6493	0.48	179	II	0.91	0.08	p	SDSS J155627.42+553857.4	G	22.67r'	0.22
J1556+5342	239.1211	53.7064	0.60	24	II	0.71	0.03	p	SDSS J155629.05+534222.9	G	22.63r'	0.26
J1556+5430	239.1267	54.5048	0.72	177	II	1.12	0.01	p	DESI J239.1267+54.5048	G	23.28r	0.35
J1556+5353	239.1312	53.9000	0.78	77	II	0.87	0.12	p	DESI J239.1312+53.9000	G	23.31r	0.36
J1556+5314	239.1368	53.2427	2.63	156	II	0.241		s	SDSS J155632.82+531433.7	G	17.71r'	0.60
J1556+5618	239.1805	56.2996	1.38	148	II	0.340		s	SDSS J155643.33+561758.7	G	18.21r'	0.40
J1556+5407	239.1856	54.1247	1.05	152	II	0.499		s	SDSS J155644.54+540728.8	G	20.10r'	0.38
J1556+5558	239.1902	55.9771	0.50	178	II	0.83	0.22	p	DESI J239.1902+55.9771	G	23.18r	0.23
J1556+5422	239.2119	54.3713	1.12	40	II	1.50		e	CWISE J155650.86+542216.8	Qc	17.01W1	0.57
J1556+5647	239.2142	56.7877	0.67	30	II	0.91	0.08	p	DESI J239.2142+56.7877	G	22.58r	0.31
J1557+5446	239.2544	54.7722	0.70	122	I	0.73	0.07	p	DESI J239.2544+54.7722	G	22.27r	0.30
J1557+5305	239.3013	53.0949	1.24	50	II	0.61	0.03	p	SDSS J155712.32+530541.5	G	20.85r'	0.50
J1557+5442	239.3131	54.7131	0.58	90	II	0.928		s	SDSS J155715.14+544247.2	G	22.31r'	0.27
J1557+5409	239.3297	54.1571	1.87	122	II	0.81	0.32	p	DESI J239.3297+54.1571	G	22.85r	0.85
J1557+5440	239.3392	54.6711	11.20	154	I	0.047		s	SDSS J155721.39+544015.9	G	13.95r'	0.62
J1557+5448	239.3770	54.8036	1.08	34	II	0.76	0.28	p	PSO J155730.480+544812.94	G	20.68r	0.48
J1557+5402	239.4011	54.0334	0.50	11	II	1.06	0.06	p	DESI J239.4011+54.0334	G	24.37r	0.24
J1557+5622	239.4081	56.3710	0.70	178	II	1.50		e	CWISE J155737.93+562215.6	Qc	17.94W1	0.36
J1557+5527	239.4508	55.4624	0.83	122	I	0.462		s	SDSS J155748.18+552744.5	G	19.69r'	0.29
J1557+5327	239.4540	53.4701	1.64	73:	I/II	0.67	0.02	p	SDSS J155748.96+532812.3	G	21.39r'	0.69
J1557+5508	239.4560	55.1401	0.65	111	I/II	1.90		e	CWISE J155749.44+550824.5	Qc	19.04W1	0.33
J1557+5343	239.4594	53.7261	0.83	100	II	0.312		s	SDSS J155750.24+534334.0	G	17.82r'	0.23
J1558+5403	239.5270	54.0549	0.33	137	II	1.03	0.12	p	DESI J239.5270+54.0549	G	23.51r	0.16
J1558+5554	239.5512	55.9047	0.68	68	II	1.21	0.19	p	DESI J239.5512+55.9047	G	25.00r	0.34
J1558+5633	239.5623	56.5503	0.63	92	II	0.92	0.01	p	DESI J239.5623+56.5503	G	23.42r	0.30
J1558+5558	239.5700	55.9836	0.85	48	II	0.50	0.09	p	SDSS J155816.81+555900.9	G	21.91r'	0.31
J1558+5349	239.5759	53.8298	0.50	33	II	1.03	0.16	p	DESI J239.5759+53.8298	Qc	23.46r	0.24
J1558+5303	239.6051	53.0636	1.77	40	I	0.687		s	SDSS J155825.22+530348.8	G	20.94r'	0.75
J1558+5609	239.7018	56.1579	0.45	115	I/II	1.28		p	DESI J239.7018+56.1579	Qc	19.84r	0.23
J1558+5441	239.7042	54.6902	1.08	52	I	0.27	0.03	p	SDSS J155849.00+544124.8	G	18.36r'	0.27
J1558+5317	239.7399	53.2952	0.53	161	II	0.472		s	SDSS J155857.57+531742.6	G	20.13r'	0.19
J1559+5527	239.7540	55.4503	0.40	136	II	1.16	0.64	p	SDSS J155900.96+552701.0	G	22.86r'	0.20
J1559+5704	239.7827	57.0779	1.30	172	II	0.592		s	SDSS J155907.84+570440.4	G	20.31r'	0.52
J1559+5448	239.8707	54.8169	0.70	5:	II	0.85	1.17	p	SDSS J155928.96+544900.8	G	19.86r'	0.32
J1559+5341	239.9018	53.6960	0.90	165	II	1.09	1.06	p	DESI J239.9018+53.6960	G	21.32r	0.44
J1559+5708	239.9340	57.1458	0.87	113	II	0.50	0.01	p	SDSS J155944.17+570844.9	G	20.84r'	0.32
J1559+5556	239.9753	55.9342	0.38	31	II	1.50		e	CWISE J155954.08+555603.2	Qc	18.03W1	0.19

[a] Col. (1), name of the ERG. A "C" appended to the ERG name indicates that it is a candidate, meaning that either the host itself, or its redshift, or its LAS are uncertain. Col. (2) and Col. (3), right ascension and declination (J2000) of the host galaxy in degrees. Col. (4), largest angular size in arcminutes. Col. (5) Radio position angle of the ERG in degrees; a colon appended to the RPA indicates that the measurement is uncertain. Col. (6), classification of the ERG according to the Fanaroff–Riley classification. Col. (7), redshift of the host galaxy. Col. (8), redshift error when available. Errors of the spectroscopic redshifts are not reported since they are generally more accurate than the precision we can achieve on the linear sizes. Col. (9), type of the redshift: p for photometric, s for spectroscopic and e if estimated. Col. (10), name of the host galaxy. Col. (11) type of host galaxy: galaxy (G) or QSO (Q) or candidate quasars (Qc). Col. (12), magnitude of the host galaxy in the r-band if available from the DESI DR9 photometric catalogue (r) or SDSSDR12 (r'); the label W1 and W2 indicates that the magnitude is taken from either WISEA (Cutri et al. 2012, 2013) or CWISE (Marocco et al. 2021) catalogues. Col. (13), largest linear size in Mpc.